Research Square

Preprints are preliminary reports that have not undergone peer review.
They should not be considered conclusive, used to inform clinical practice,
or referenced by the media as validated information.

Influence of Cu2Te Doping on the Microstructure and Phase Formation Process of MgB2 Superconductor

Qian Zhao

zhaoqian@tust.edu.cn

Tianjin University of Science and Technology

Hang Shen

Tianjin University of Science and Technology

Yan Xue

Tianjin University of Science and Technology

Guo qing Xia

Tianjin University of Science and Technology

Jiabo Zhang

Tianjin University of Science and Technology

Shilong Ma

Tianjin University of Science and Technology

Hao Liang

The University of Queensland

Yaran Zhang

Xingtai University

Research Article

Keywords: MgB2 superconductors, Cu2Te doping, Liquid-phase sintering, Flux pinning, Critical current density

Posted Date: August 10th, 2026

DOI: https://doi.org/10.21203/rs.3.rs-10457845/v1

License: This work is licensed under a Creative Commons Attribution 4.0 International License.
Read Full License

Additional Declarations: No competing interests reported.

Influence of Cu_2Te Doping on the Microstructure and Phase Formation Process of MgB_2 Superconductor

Qian Zhao[a,*], Hang Shen[a], Yan Xue[a], Guoqing Xia[a], Jiabo Zhang[a], Shilong Ma[a], Hao Liang[b], Yaran Zhang[c,*]

[a]*Tianjin Key Laboratory of Integrated Design and On-line Monitoring for Light Industry & Food Machinery and Equipment, School of Mechanical Engineering, Tianjin University of Science and Technology, Tianjin 300457, People's Republic of China*

[b]*School of Mechanical and Mining Engineering, The University of Queensland, St Lucia, Queensland 4072, Australia*

[c]*College of Physics and Electronic Engineering and Hebei Technology Innovation Center for Digital-Intelligent Rescue Equipment, Xingtai University, Xingtai 054001, China*

**Corresponding author. E-mail address: zhaoqian@tust.edu.cn, yaranzhang@126.com*

Abstract: Cu_2Te-doped MgB_2 bulks were synthesized to systematically investigate the effects of doping on phase formation thermodynamics, microstructure, and superconducting properties. The study reveals that the introduction of Cu_2Te significantly alters the reaction process of MgB_2. The Mg-Cu eutectic liquid phase, formed at approximately 485 ℃ from the decomposition of Cu_2Te, serves as a rapid atomic diffusion channel, which significantly reduces the phase formation temperature of MgB_2 and promotes sintering densification. Microstructural characterizations confirm that the enhancement of superconducting properties originates from the synergistic effect of dual microstructural mechanisms. On the one hand, an appropriate amount of doping effectively refines the MgB_2 grains and improves intergranular connectivity; on the other hand, MgTe and $MgCu_2$ nanoparticles (10-50 nm) with sizes matching the superconducting coherence length can also act as efficient flux pinning centers. Experimental results indicate that the optimal doping amount of Cu_2Te is 2 wt%, and the J_c value at 20 K self-field reaches 2.3×10^5 A·cm^{-2}, an increase of about 15% compared to pure MgB_2. Thus, the introduction of Cu_2Te successfully transforms the dominant phase formation mechanism of MgB_2 from a traditional high-temperature liquid-solid reaction to a low-temperature eutectic liquid-assisted reaction pathway.

Keywords: MgB_2 superconductors; Cu_2Te doping; Liquid-phase sintering; Flux pinning; Critical current density

1. Introduction

The discovery of MgB_2 superconductor in 2001, has emerged as a highly promising candidate for large-scale applications within the 20-30 K regime. This prospect is heavily driven by its compelling intrinsic properties, including a high critical transition temperature (T_c=39 K), essentially isotropic nature, and remarkable cost-effectiveness[1-2]. Nevertheless, the practical deployment of MgB_2 in high-field applications is profoundly hindered by poor intergranular connectivity and an inherently weak flux pinning capability. Consequently, its critical current density (J_c) experiences a precipitous decline as the external magnetic field increases[3].

Researchers have employed various methods such as spark plasma sintering, irradiation, chemical doping, and high-pressure densification to improve its superconducting properties and enhance the current-carrying capacity of MgB_2 under high magnetic fields[4-7]. Studies by Gajda et al.[8-10]demonstrated that high-pressure sintering can significantly improve performance; however, its high preparation cost limits its viability for large-scale industrial production. In contrast, chemical doping is considered as a more practical and efficient modification approach due to its simplicity and effectiveness. Early modification research primarily focused on further increasing T_c by tuning the electronic structure of MgB_2. However, the unique two-band structure of MgB_2 means that lattice substitution by most elements tends to suppress T_c. Research indicates that only a few metallic elements, such as Li, Al, and Be, can achieve effective hole or electron doping[11-13]. As an element in the same group as Mg or with a similar atomic radius, Al can partially substitute at the Mg site, causing the lattice parameters a and c to shrink and inducing lattice distortion, which somewhat improves the low-field current-carrying capacity[14]. Nevertheless, as the doping level increases, the strong scattering effect introduced by Al leads to a significant decrease in pinning force, ultimately deteriorating the upper critical field (H_{c2}) and J_c. Substitutional doping with elements like La, Na, Ca, and Ti[15-18] exhibits similar limitations, making it difficult to achieve breakthroughs in high-field performance.

With a deeper understanding of the phase formation mechanism of MgB_2, the research focus has gradually shifted towards introducing secondary phase particles via additives to enhance flux pinning, or improving intergranular connectivity through liquid-phase assisted sintering. Flux pinning refers to the phenomenon where magnetic flux quanta in a superconductor are trapped by localized defects or interfaces under an external magnetic field, inhibiting their motion to effectively increase J_c and maintain superconducting stability. General mechanisms include point pinning and surface pinning; the former is achieved by doping nanoparticles or introducing lattice defects, while the latter relies on energy barriers formed by grain boundaries and phase interfaces. For instance, Dou et al. [19-21]demonstrated that incorporating nano-SiC can introduce pinning centers directly into the grains, significantly enhancing the pinning effect. Wang et al.[22] synthesized $Mg_{0.5}Cd_{0.5}B_2$ in situ and found that the generated $MgCd_3$ impurity phase acts as effective pinning centers, enabling the sample to achieve a J_c of 5.0×10^5 A·cm^{-2} under a 5 K self-field. Muralidhar et al. [23] utilized Ag doping to generate the $AgMg_3$ phase, achieving a substantial increase in self-field J_c. Regarding connectivity improvements, Chen et al.[24] reported that Ga doping forms Mg-Ga eutectic liquid phase at a low temperature of 422 °C, which effectively fills pores and increases the 20 K J_c by 10 times compared to the pure sample. Ma et al.[25] further confirmed that Cu doping displays the similar liquid-phase activation: Cu reacts with Mg at 485 °C to form an Mg-Cu eutectic liquid, providing a rapid diffusion channel for Mg into B, which accelerates the phase formation rate and promotes the development of the dense lamellar structures.

Currently, researchers are increasingly focusing on the synergistic regulation of flux pinning and intergranular connectivity to overcome the performance bottlenecks of MgB_2. Zhao et al.[26] utilized Ti doping to construct nanoscale TiB_2 layers at grain

boundaries, achieving the multiple effects of refining grains, enhancing connectivity, and providing pinning centers. In previous work, our group systematically investigated the effects of micrometer-scale Ni powder on MgB_2[27][28]. The results showed that the formed Ni-Mg eutectic liquid phase at 506 °C significantly improved sintering neck connections, and $MgNi_{2.5}B_2$ particles within the MgB_2 grains effectively prevented the concentration of impurities at the grain boundaries. Nevertheless, the restricted current density is attributed to the magnetic nature of Ni. Although elemental metallic doping has yielded numerous achievements in recent years, it still presents substantial limitations. Due to doping proportion constraints, even if metallic elements form a eutectic liquid phase with Mg, the minimal volume of this liquid means the majority of the Mg-B reaction still occurs above 650 °C. The volatilization of Mg at the high temperature generates numerous voids in the sample, suppressing the benefits of low-temperature liquid-phase assisted sintering. Consequently, effectively increasing the low-temperature formation rate of MgB_2 and further reducing high-temperature Mg volatilization has become an urgent issue for improving intergranular connectivity. Our group previously explored Cu_2Se as a dopant and systematically studied its impact on microstructure and superconductivity[29]. Results indicated that Cu_2Se reacts with Mg to form Mg_2Cu and MgSe secondary phases at 520 °C. The consumed Mg has further reduced Mg volatilization during the high-temperature reaction stage. Subsequently, Mg_2Cu reacts with B to form MgB_2 and $MgCu_2$ at 620 °C. The exothermic reaction between Mg and Cu_2Se promotes the early onset of MgB_2 formation. This mechanism spans the entire sintering process, allowing the reaction to complete entirely at 630 °C. Compared to traditional pure MgB_2 sintered at 750 °C, the low-field J_c was significantly improved, further confirming that the dopant type largely dictates the density of the superconducting sample.

Building upon the foundation of Cu_2Se doping, and considering that tellurium (Te) and selenium (Se) belong to the same chalcogen group but Te possesses a larger atomic radius, it is hypothesized that Te may induce different phase transition pathways while simultaneously enhancing the pinning strength. In consequence, Cu_2Te is selected as a novel doping element in this study to deeply investigate its effects on the sintering process, microstructure, and superconducting properties of MgB_2. While doping with most elements can improve critical current performance under high magnetic fields, it typically struggles to simultaneously enhance low-field performance, which is closely related to the effective intergranular connection area. Therefore, this experiment introduces Cold Isostatic Pressing (CIP) technology for sample densification, expecting to obtain MgB_2 samples with higher relative density and thereby improve low-field current performance. During the experiment, the raw material ratio is adjusted by increasing the Mg powder content to an atomic ratio of n(Mg):n(Cu)=4:1, compensating for Mg consumption during the reaction and improving the material's superconducting properties. This paper will focus on exploring the intrinsic mechanisms by which the Cu_2Te-induced step-by-step phase formation process suppresses Mg volatilization, optimizes the micro-pore structure, and tunes flux pinning behavior, aiming to synthesize high-performance MgB_2 superconduct or featuring both high density and strong pinning characteristics.

2. Experiments

Cu_2Te-doped MgB_2 bulk superconductors were synthesized via a conventional in-situ solid-state reaction route. Commercially available high-purity Mg powder (≥ 99.9%, 40 μm), amorphous B powder (≥99%, 20 μm), and Cu_2Te powder (≥99.5%) were utilized as the raw materials. The specific preparation process is as follows:

Based on the stoichiometric ratios and mass fractions detailed in Table 1, the precursor powders were manually ground in an agate mortar for 30 min to achieve an atomic-scale homogeneous dispersion of the multiphase components. The blended powders were then loaded into a 5 mm-diameter steel die and uniaxially pre-pressed at 5 MPa into cylindrical pellets (Φ5×1.5 mm). To prevent oxidation and maximize the green density, the pre-pressed pellets were vacuum-sealed and subjected to cold isostatic pressing (CIP) up to 300 MPa. To alleviate internal residual stresses within the green bodies, a step-wise pressurization protocol was applied, increasing the pressure by 100 MPa every 2 min with a 1-min dwell time at each increment. Subsequently, the densified pellets were sintered in a tube furnace under a continuous flow of high-purity argon. The thermal profile consisted of heating from room temperature to 750 ℃ at a ramp rate of 20 ℃·min^{-1}, followed by an isothermal hold for 0.5 h, and concluding with furnace cooling to ambient temperature. According to their respective Cu_2Te doping concentrations (0,2,5,10, and 20 wt%), the resulting samples are hereafter designated as CT-0, CT-2, CT-5, CT-10, and CT-20.

Table 1 Overview of the MgB_2 samples containing 0~20 wt% Cu_2Te and the sintering profile

Sample name	Sample	Temperature/°C	Duration/h	Size/mm
CT-0	MgB_2			
CT-2	MgB_2+2 wt% Cu_2Te			
CT-5	MgB_2+5 wt% Cu_2Te	750	0.5	Φ5×1.5
CT-10	MgB_2+10 wt% Cu_2Te			
CT-20	MgB_2+20 wt% Cu_2Te			

Phase identification of the sintered samples was performed using an X-ray diffractometer (XRD, Bruker D8 Advance, Germany). For microstructural observation was examined by scanning electron microscope (SEM, Hitachi S4800). Transmission electron microscopy (TEM, JEM 2100F) coupled with selected area electron diffraction (SAED) was employed to evaluate the size and chemical composition of the dark precipitates within the doped specimens. The phase formation process was monitored using a simultaneous thermal analyzer (DSC, STA200Regulus). For electromagnetic characterization, the cylindrical samples were mechanically polished with abrasive paper into rectangular prisms with dimensions of 3×2×1 mm^3. The magnetic properties of the MgB_2-based composites were measured using a Magnetic Property Measurement System (SQUID-VSM, MPMS3, Quantum Design, USA). Measurements were conducted in a standard DC magnetization mode at 20 K (facilitated by a closed-cycle liquid helium cryostat). A sweeping magnetic field from -7 T to 7 T was applied parallel

to the longest axis of the specimens to acquire quasi-static magnetic hysteresis (*M-H*) loops. The magnetic field dependence of the critical current density (J_c-*H*) was derived using the Bean critical state model[30] via the formula: $J_c=20\Delta M/abh^2[1-h/(3b)]$. Where ΔM is the difference in magnetization between the upper and lower branches of the hysteresis loop at a given field (in emu), *a* is the length of the longest edge of the rectangular prism, and *h* and *b* are the lengths of the shorter edges ($h<b$), all in mm.

3. Result and discussions

To clarify the impact of Cu_2Te doping on the phase composition of MgB_2, the X-ray diffraction (XRD) patterns of the samples were qualitatively analyzed using Jade software, as depicted in Fig. 1. The results reveal that MgB_2 remains the dominant matrix phase across all samples, although its diffraction peak intensities exhibit a distinct systematic evolution with increasing dopant concentration. Concurrently, typical MgO diffraction peaks are invariably detected in all spectra. This originates primarily from the inherent high chemical reactivity of elemental Mg; despite the vacuum-sealed sintering environment, trace oxygen adsorbed by the precursor powders during the initial grinding and transferring processes is sufficient to trigger mild oxidation, yielding a minor MgO impurity phase. In contrast to pure MgB_2, the Cu_2Te-doped samples feature two newly emergent secondary phases: MgTe and $MgCu_2$. The complete absence of Cu_2Te diffraction peaks confirms its total consumption via solid-state reactions during sintering. Notably, Fig. 1 demonstrates a significant attenuation in the main MgB_2 diffraction peak intensity for the CT-2 sample, accompanied by a pronounced broadening of the full width at half maximum (FWHM). According to the Scherrer equation, this indicates an effective refinement of the MgB_2 crystallite size and a relative reduction in crystallinity at this specific doping level. Conversely, the MgB_2 peak intensity in the CT-20 sample recovers, displaying sharpened profiles without evident broadening. This suggests that excessive dopant addition may paradoxically induce grain coarsening of the matrix phase. The mechanistic origins of this phenomenon and its implications for superconducting performance will be comprehensively discussed in subsequent sections, corroborating with SEM characterizations and electromagnetic measurements.

Table 2 summarizes the microstructural constitutive parameters of the composite samples with varying Cu_2Te doping levels, which display a compelling correlation with the electromagnetic characteristics. For the CT-2 sample, which exhibits the optimal superconducting performance, the lattice parameters, where *a* equals 3.0863Å and *c* equals 3.5259Å, remain remarkably close to those of the pristine MgB_2. This implies that a moderate introduction of Cu_2Te preserves the intrinsic crystalline integrity of the MgB_2 matrix, thereby maintaining a high active superconducting volume fraction. Intriguingly, the CT-2 sample demonstrates an anisotropic FWHM evolution, wherein a localized minimum of 0.250° is observed for the (002) peak alongside a broadened (110) peak. This anisotropic behavior suggests that the transient appearance of the Mg-Cu eutectic liquid phase selectively moderates the grain growth kinetics of MgB_2 along specific crystallographic orientations during the incipient stage of sintering. Beyond this optimal threshold, which is greater than or equal to 5 wt%, the generalized

broadening of FWHM, as exemplified by the (002) peak of the CT-5 sample reaching 0.519°, is primarily ascribed to the prominent strain fields generated by the burst-like precipitation of boundary MgTe and $MgCu_2$ nanoparticles. Ultimately, the catastrophic collapse of lattice parameters coupled with the maximum (110) FWHM of 0.388° in the CT-20 sample convincingly underpins its severe high-field J_c degradation, stemming from severe structural disorders and the severe curtailment of effective superconducting connectivity.

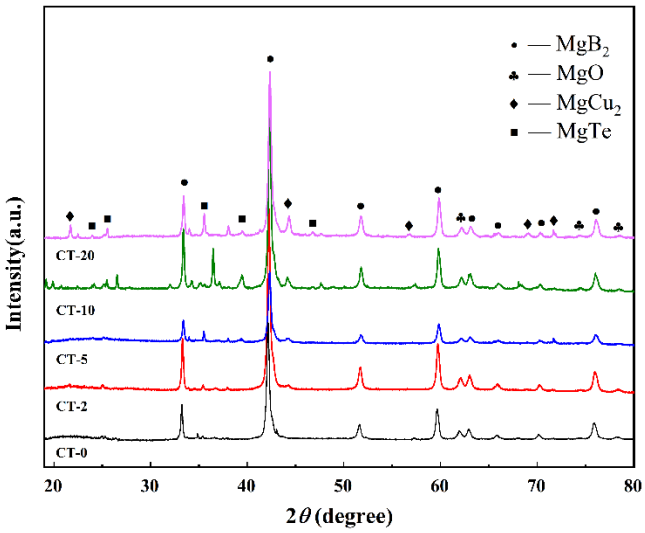


Fig. 1. X-ray diffraction pattern of the samples sintered at 750 °C for 30 min

Table 2 Lattice parameters, characteristic peak positions, and FWHM of composite samples with varying Cu_2Te doping levels

Sample	*a*/Å	*c*/Å	2θ of (002) peak	2θ of (110) peak	FWHM of (002) peak	FWHM of (110) peak
CT-0	3.0859	3.5230	51.876	59.935	0.324	0.266
CT-2	3.0863	3.5259	51.860	59.919	0.250	0.314
CT-5	3.0864	3.5215	51.933	59.907	0.519	0.316
CT-10	3.0865	3.5217	51.907	59.865	0.390	0.338
CT-20	3.0811	3.5157	51.921	59.884	0.382	0.388

Furthermore, to quantitatively assess the impact of phase evolution on the effective superconducting cross-sectional area, the phase volume fractions derived from peak area integrations are plotted in Fig. 2. It is evident that the proportion of the dominant MgB_2 phase undergoes a precipitous decline as the dopant concentration increases, while the volume fraction of MgO remains relatively stable across various doping levels. This systematic trend provides compelling evidence of a fierce competitive reaction between the Cu and the Mg matrix. Consequently, this competitive mechanism not only

exhausts the intentionally supplemented excess Mg but also scavenges the Mg atoms inherently destined for MgB_2 formation to precipitate $MgCu_2$, ultimately resulting in a macroscopic deterioration of the overall MgB_2 phase yield.

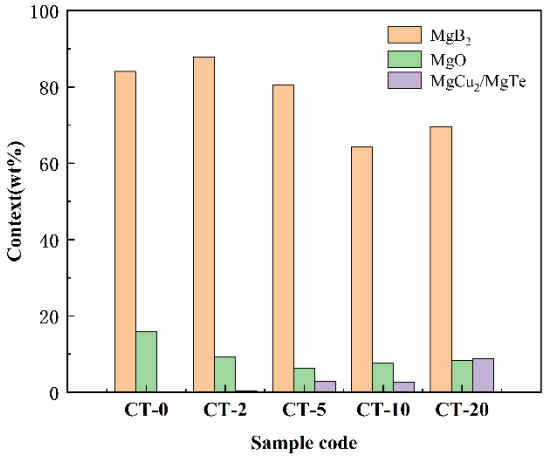


Fig. 2. The volume fraction of each phase in doped Cu_2Te samples

Fig. 3 presents the microstructural evolution of the MgB_2 bulks with varying Cu_2Te doping concentrations as observed by SEM. A pronounced densification transition is evident upon increasing the dopant level. The microstructures of the lightly doped specimens (CT-2 and CT-5) are characterized by an abundance of irregular pores and microcracks, indicative of severe internal porosity. At these lower doping levels, the limited volume fraction of the in-situ generated Mg-Cu eutectic liquid restricts the kinetic benefits of liquid-phase assisted sintering. Consequently, the sluggish diffusion of Mg atoms toward the B matrix leaves behind a proliferation of voids induced by the Kirkendall effect and volumetric shrinkage. Conversely, at higher doping levels (CT-10 and CT-20), the pore density undergoes a precipitous decline accompanied by a highly compacted granular stacking. This compellingly demonstrates that the liquid phase effectively drives the densification process and substantially ameliorates intergranular connectivity.

In the lightly doped state, the primary matrix grains predominantly agglomerate into fine, irregular clusters, lacking the quintessential hexagonal platelet morphology. This microstructural feature perfectly corroborates the XRD results, where the CT-2 specimen displayed the most pronounced peak broadening, definitively confirming substantial grain refinement. Additionally, high-magnification SEM (Fig. 3(b)) reveals distinct, highly bright nanoscale particles decorating the grain boundaries and pore perimeters. Correlating these observations with the XRD phase analysis and electron contrast mechanisms established in the literature[22][23][25], these bright contrast regions are identified as $MgCu_2$ secondary phases and dielectric MgO particles susceptible to charge accumulation. Strikingly, the population of these oxide-related bright spots systematically diminishes with increased Cu_2Te doping (Fig. 3(c)). Mechanistically, the transient Mg-Cu local liquid phase encapsulates the nascent MgB_2 grains, establishing a robust physical barrier that isolates the reactive Mg matrix from residual oxygen. This in-situ protective mechanism suppresses oxidation far more effectively than conventional thermal protocols aimed at balancing crystallinity against oxidation.

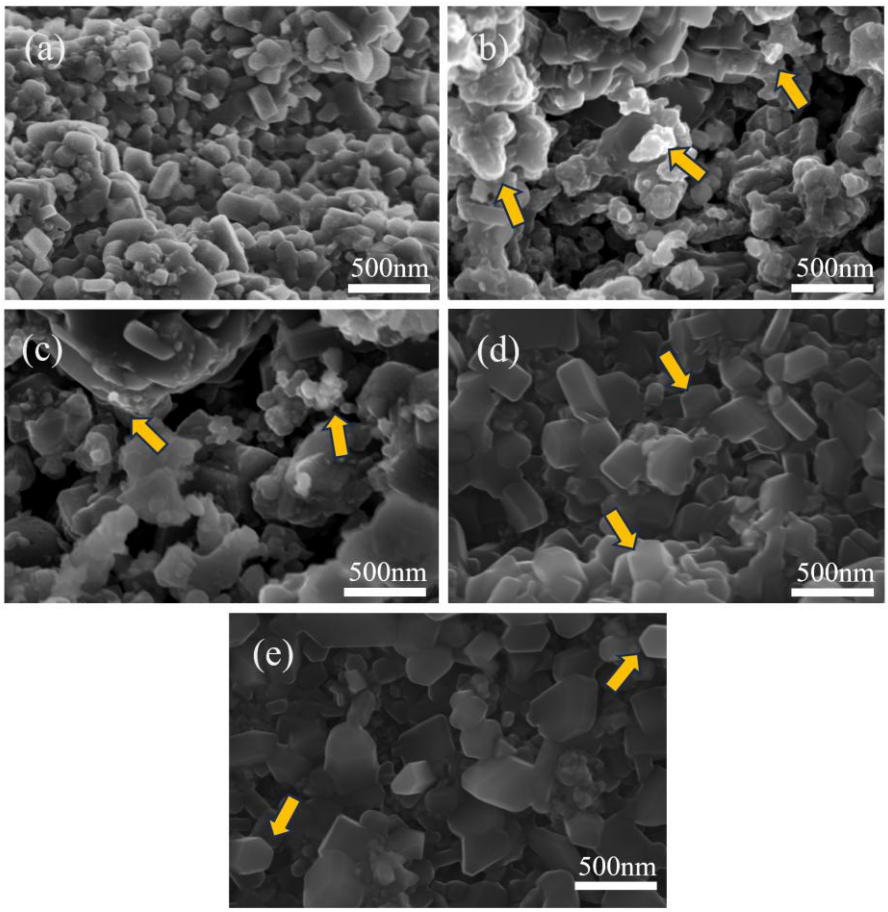


Fig. 3. SEM images of pure MgB_2 and Cu_2Te doped samples: (a) CT-0，(b) CT-2，(c) CT-5，(d) CT-10, (e) CT-20

By stark contrast, the microstructures of the heavily doped CT-10 and CT-20 specimens undergo a profound transformation. The copious liquid-phase environment drastically accelerates the mass transfer rate, facilitating the fully-fledged growth of MgB_2 grains into well-defined, intact hexagonal architectures. As depicted in the high-magnification images (Fig. 3(d,e)), the crystallites manifest striking lamellar stacking or “step-like” growth characteristics. This morphological paradigm deviates radically from the smooth facets typical of conventional solid-state sintering, unraveling a unique crystal growth kinetic mechanism. Within this Cu_2Te-activated, low-temperature liquid-phase sintering regime, the crystallization of MgB_2 is predominantly governed by a screw dislocation-driven nucleation mechanism[31]. Impurity atoms or nanoscale secondary phases dispersed in the liquid phase preferentially adsorb onto the growth steps of the crystal surfaces, functioning as nascent step sources that catalyze the evolution of this terraced morphology. Consequently, this proliferation of grain boundaries and intricate surface step configurations is highly anticipated to furnish an abundance of potent magnetic flux pinning centers.

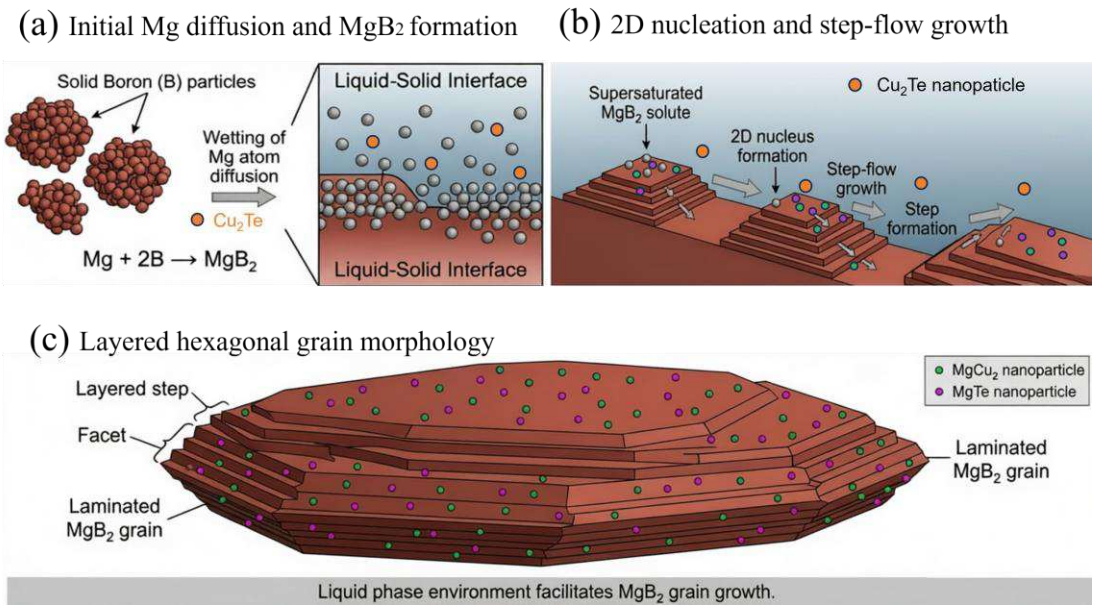


Fig. 4. Schematic diagram of the formation mechanism of layered MgB_2 crystal structure. Among them, (a) the initial stage, (b) the nucleation growth stage, and (c) the final stage

The schematic in Fig. 4 systematically elucidates the stepwise growth kinetics model of lamellar MgB_2 crystals facilitated by the transient Mg-Cu liquid phase. This kinetic process is fundamentally governed by solute diffusion within the melt coupled with interfacial reactions. Initially (Fig. 4(a)), as the Mg-Cu melt wets the solid B particles, Mg atoms rapidly diffuse through the liquid conduit toward the reaction interface. The localized consumption of Mg to synthesize MgB_2 engenders a steep Mg concentration gradient within the liquid phase. This chemical potential gradient serves as a potent driving force, propelling the continuous flux of Mg toward the reaction front. As the synthesis proceeds (Fig. 4(b)), the MgB_2 solute concentration within the melt escalates, ultimately reaching supersaturation. Dictated by classical crystal growth theory[32], once this supersaturation breaches the critical threshold for two-dimensional nucleation, nascent nuclei precipitate via thermodynamic fluctuations on either the unreacted B substrate or preexisting facets, subsequently propagating laterally via step epitaxy. Consequently (Fig. 4(c)), upon the completion of a monolayer terrace, successive nucleation ensues atop the newly formed facet, perpetuating a cyclic growth regime. This canonical "dissolution-diffusion-precipitation" mechanism inherently dictates the formation of MgB_2 crystallites characterized by pronounced lamellar stacking, impeccably corroborating the terraced morphologies visualized via SEM. The copious liquid environment drastically accelerates mass transport, fostering the fully-fledged development of distinct, unblemished hexagonal architectures. During this stepwise propagation, the accompanying secondary phases ($MgCu_2$ and MgTe) within the liquid are dynamically expelled to the advancing growth fronts, ultimately depositing as a fine dispersion of nanoparticles decorating the grain boundaries of the hexagonal MgB_2 matrix.

To further precisely localize and chemically identify these impurity phases within the microstructural framework, Energy Dispersive X-ray Spectroscopy (EDS) elemental mapping was conducted on the CT-20 specimen (referencing Fig. 3(e)), as

delineated in Fig. 5. The elemental spatial distributions (Fig. 5(a, b)) unequivocally reveal that Cu and Te are not homogeneously incorporated; rather, they exhibit pronounced localized segregation, as highlighted by the dashed red enclosures. Correlating these maps with the corresponding SEM topography confirms that these segregated zones are exclusively confined to the MgB_2 grain boundaries or particulate peripheries, with a stark absence of Cu and Te signals within the crystal interiors. Integrated with the global spectrum (Fig. 5(c)), which confirms a composition dominated by Mg and B, alongside trace Cu, Te, and O, these findings compellingly substantiate the XRD deductions. Specifically, the Cu and Te dopants are entirely excluded from substituting into the intrinsic MgB_2 lattice; instead, they precipitate in-situ as discrete $MgCu_2$ and MgTe secondary phases pinned at the intergranular interfaces. This distinctive "intragranularly pristine, intergranularly enriched" architectural paradigm confers a profound dual benefit: firstly, the dynamic expulsion of the liquid phase during terraced growth guarantees the exceptional crystallinity of the superconducting matrix; secondly, the intergranular dispersion of these non-superconducting nanoprecipitates ($MgCu_2$ and MgTe) provides a high density of robust flux pinning centers, an indispensable prerequisite for elevating the critical current density (J_c) under intense magnetic fields.

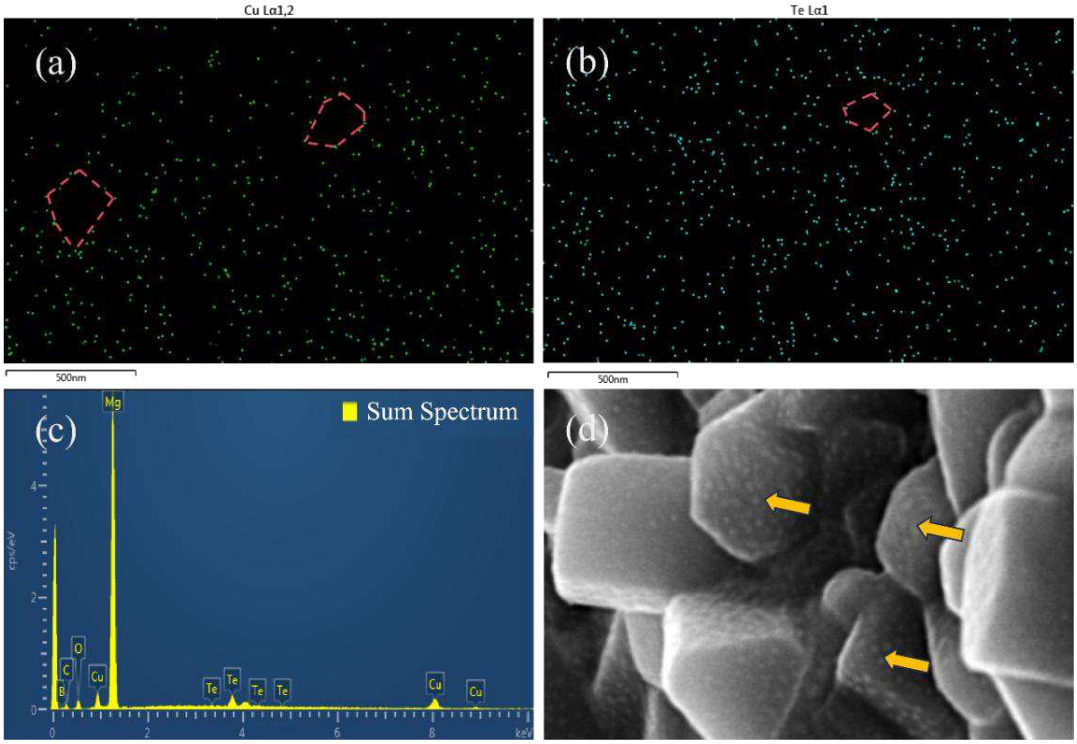


Fig. 5. Elemental distribution of CT-20: (a) Cu element distribution map, (b) Te element distribution map, (c) element scale map (d)Secondary nanoparticles on surface

To fully elucidate the nanoscale morphology, crystallographic structure, and interfacial relationships of the secondary phases with the MgB_2 matrix, transmission electron microscopy (TEM) and high-resolution TEM (HRTEM) characterizations were conducted on the CT-20 specimen, as depicted in Fig. 6. The bright-field micrograph (Fig. 6(a)) unequivocally reveals an abundance of high-contrast nanoparticles uniformly dispersed throughout the MgB_2 matrix. Strikingly, the

dimensions of these secondary phase precipitates (spanning 10-50 nm) perfectly match the scale of the superconducting coherence length of MgB_2. Dictated by flux pinning theory, defects approaching this critical length scale yield the most robust pinning force. Consequently, these nanoprecipitates hold immense promise as optimal flux pinning centers, which is anticipated to drastically elevate the high-field J_c of the bulk MgB_2. The corresponding selected area electron diffraction (SAED) pattern (Fig. 6(c)) displays distinct concentric rings, corroborating the polycrystalline nature of the local region. Indexed via Bragg's law ($2dsin\theta = \lambda$) and referenced against standard PDF cards, these diffraction rings are unambiguously assigned to the (101) and (200) planes of the MgB_2 matrix, alongside the (110) plane of MgTe and the (511) plane of $MgCu_2$. This crystallographic evidence conclusively verifies that the dark nanoscale precipitates dispersed within the matrix are indeed MgTe and $MgCu_2$, in perfect agreement with the aforementioned XRD deductions.

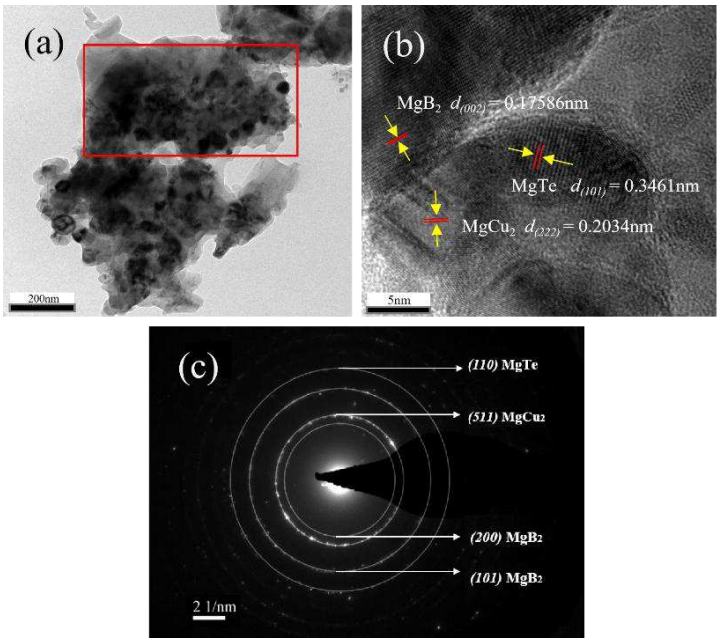


Fig. 6. TEM image and SAED diffraction pattern of CT-20

Subsequent HRTEM examination of these dark particulate regions (Fig. 6(b)) resolves distinct lattice fringes, signifying exceptional crystallinity across all constituent phases. The measured interplanar d-spacings of 0.2034 nm and 0.3461 nm are precisely indexed to the (222) plane of cubic $MgCu_2$ and the (101) plane of hexagonal MgTe, respectively. Concurrently, the (002) lattice fringes of the MgB_2 matrix ($d = 0.1758$ nm) are also clearly resolved. Morphologically, the marginally larger size of MgTe relative to $MgCu_2$ hints at a divergence in their respective crystallization kinetics: it is hypothesized that MgTe preferentially nucleates and coarsens during the initial reaction stages, whereas $MgCu_2$ precipitates in tandem with the concurrent evolution of the MgB_2 matrix. Crucially, these nanoprecipitates establish tightly bound, coherent interfaces with the surrounding MgB_2 matrix. Such interfacial coupling is highly advantageous, as it induces localized lattice distortions to effectively anchor magnetic flux lines, without compromising the intergranular percolation pathways

essential for unhindered superconducting current transport.

To thoroughly investigate the influence of Cu_2Te doping on the phase formation reaction pathway of MgB_2, the sintering process of the mixed powder was characterized by differential scanning calorimetry (DSC) in this experiment. To preclude high-temperature oxidation, the thermal analysis was performed under a continuous flow of high-purity argon at a constant heating rate of 20 °C·min^{-1}. Fig. 7 presents the DSC thermograms of both the pristine and Cu_2Te-doped MgB_2 samples. While the doped specimens exhibit markedly altered reaction profiles relative to the pristine baseline, the overarching thermal behavior is governed by three principal thermodynamic events. These comprise an initial exothermic peak at approximately 540 °C, attributed to the Mg-B solid-solid diffusion reaction or nascent localized liquid-phase interactions; a prominent endothermic peak near 645 °C, representing the melting of elemental Mg; and a subsequent second exothermic peak around 665 °C, signifying the vigorous liquid-solid reaction between the molten Mg and the B matrix.

The DSC curves in Fig. 7 indicate that the introduction of Cu_2Te significantly changes the thermodynamic synthesis pathway of MgB_2. Compared with the undoped CT-0 sample, the initial reaction temperatures of all doped samples shift towards the low-temperature. This phenomenon can be attributed to the Mg-Cu eutectic liquid phase, which provides a rapid channel for the diffusion of Mg into B, thereby effectively lowering the synthesis reaction temperature of MgB_2. In the high-doping CT-10 and CT-20 samples, the sharpness of the Mg melting endothermic peak decreases significantly and even nearly disappears. This implies that a large amount of solid Mg has been consumed through low-temperature reactions before its melting point. Meanwhile, the large amount of heat released by the low-temperature exothermic reaction effectively compensates for the latent heat of melting of the remaining Mg, leading to the blunting of its endothermic peak features. In addition, as the doping amount increases, the intensity of the low-temperature exothermic peak (Peak 1) becomes significantly higher than that of the high-temperature exothermic peak (Peak 3), which intuitively proves the migration of the main reaction zone from high temperatures to low temperatures. In summary, the introduction of Cu_2Te successfully transforms the dominant phase formation mechanism of MgB_2 from the traditional high-temperature liquid-solid reaction to a low-temperature eutectic liquid-assisted reaction pathway.

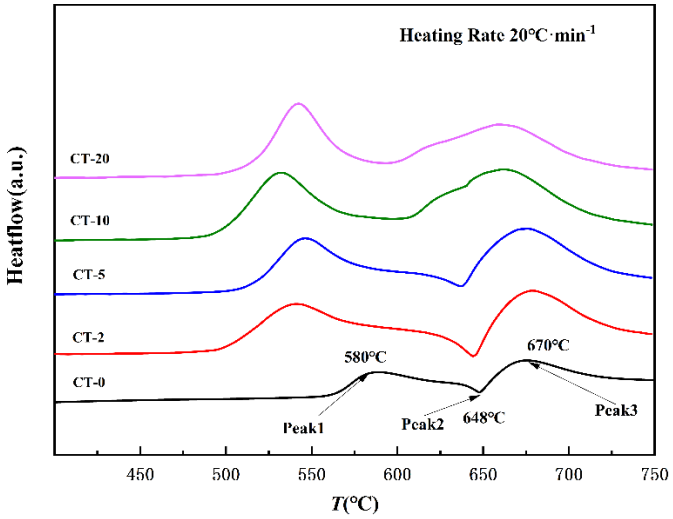


Fig. 7. DSC curves recorded during the sintering process of Cu_2Te doped MgB_2 samples

To systematically deconvolute the overlapping thermal signals and precisely elucidate the reaction pathway of the Cu_2Te-doped system, the CT-20 specimen was subjected to DSC analysis at multiple heating rates of 5, 10, and 20 °C·min^{-1}. This was complemented by interrupted sintering experiments and subsequent XRD phase tracking at characteristic temperatures (450, 550, and 650 °C), as depicted in the results. Fig. 8(a) reveals that varying the heating rate clearly demonstrates the kinetic characteristics of the phase transition process; as the heating rate increases, both exothermic peaks systematically shift toward higher temperatures. Specifically, at a lower heating rate of 5 °C·min^{-1}, which provides the highest thermal resolution, the originally broadened exothermic trace successfully bifurcates into two distinct and independent reaction stages: a primary exothermic peak (Peak 1) centered at approximately 490 °C and a secondary exothermic peak (Peak 3) at approximately 623 °C. Correlating these thermal events with the temperature-dependent XRD profiles (Fig. 8(b)) allows the phase formation process of Cu_2Te-doped MgB_2 to be delineated into two critical stages.

The first stage involves a low-temperature solid-state reaction (below 490 ℃) and the precipitation of intermediate phases. During the sintering process, as the temperature reaches 450 ℃, Mg initially undergoes a solid-state displacement reaction with Cu_2Te: $Mg(s) + Cu_2Te(s) \rightarrow MgTe(s) + 2Cu(s/l)$ (Peak 1). As the temperature further escalates to 485 ℃, the partial Mg and Cu form a localized Mg-Cu eutectic liquid phase. This transient liquid acts as a high-speed diffusion conduit for Mg into the B matrix, thereby advancing the solid-state synthesis of MgB_2 to 550 ℃ (as depicted in Fig. 8(b)). The rapid exhaustion of Mg during this low-temperature regime perfectly accounts for the absence of a distinct Mg melting endotherm in the DSC curve. Subsequently, the eutectic liquid phase is consumed to further form Mg_2Cu. Given that this is a vigorous exothermic process yielding a substantial phase fraction, the Mg_2Cu phase is clearly detected in the XRD pattern of the sample sintered at 550 ℃, further corroborating the occurrence of this reaction pathway.

The second stage is characterized by the transformation of intermediate phases and the explosive growth of the primary phase. Upon heating to 623 °C (Peak 3), the XRD

patterns reveal the complete dissolution of the Mg_2Cu peak, succeeded by the emergence of the stable $MgCu_2$ phase. Concurrently, the diffraction intensity of MgB_2 experiences a dramatic surge. This microstructural evolution corresponds to the secondary reaction between the Mg_2Cu intermediate and the residual B precursor: $2Mg_2Cu(s/l) + 6B(s) \rightarrow 3MgB_2(s) + MgCu_2(s)$, This progressive liberation of Mg atoms from the Mg_2Cu intermediate to actively participate in the MgB_2 synthesis significantly amplifies the volume fraction of the primary superconducting matrix. In summary, the incorporation of Cu_2Te fundamentally circumvents the singular "Mg melting-liquid diffusion" pathway inherent to pure MgB_2 systems, establishing a distinctive "stepwise consumption and in-situ formation" paradigm. Firstly, the vast majority of elemental Mg is aggressively consumed to form MgB_2 or intermediate phases via solid-state or eutectic reactions well below its macroscopic melting point (650 ℃). This "react-before-melting" regime elegantly mitigates the formation of large macroscopic voids typically induced by the volumetric shrinkage and severe volatilization of liquid Mg at elevated temperatures, thereby fundamentally reinforcing the densification and intergranular connectivity. Secondly, the reaction byproducts, MgTe and $MgCu_2$, precipitating in-situ along the MgB_2 grain boundaries at low temperatures, their growth is sterically confined by the primary matrix boundaries, thereby retaining nanoscale dimensions. As corroborated by the preceding TEM analysis, these finely dispersed nanoparticles effectively compensate for the reduction in grain boundary density induced by matrix grain coarsening, furnishing abundant additional flux pinning centers. Consequently, this establishes a robust microstructural architecture where superior intergranular connectivity and potent flux pinning synergistically coexist.

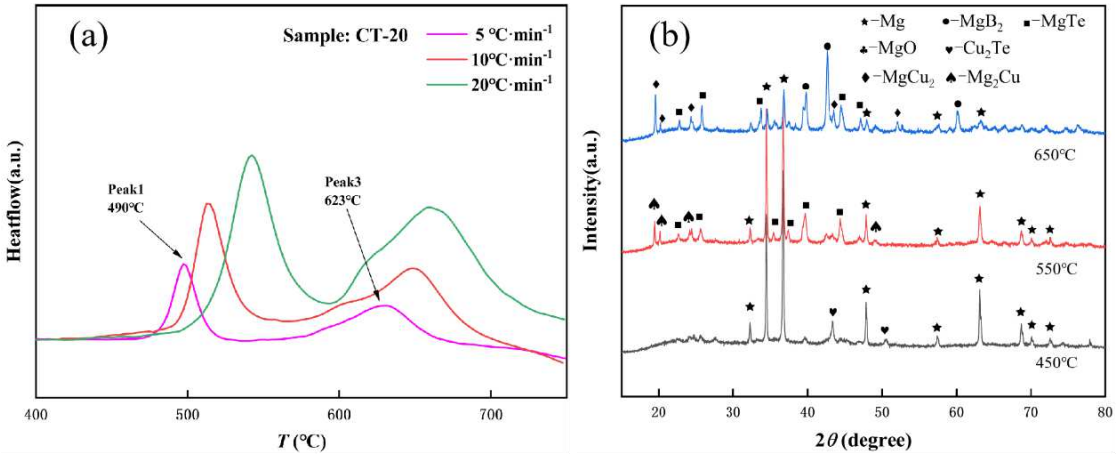


Fig. 8. (a) DSC curves and (b) XRD patterns of the CT-20 under various sintering process

The reduced magnetization versus temperature curves of the MgB_2 bulks with varying Cu_2Te doping levels are database depicted in Fig. 9(a), and the corresponding critical transition temperature values are summarized in Fig. 9(b). It can be observed that the critical transition temperature of the pristine sample is approximately 38.53 K. Upon the introduction of Cu_2Te doping, the critical transition temperatures experience a slight decrease, where the values for the CT-2, CT-5, CT-10, and CT-20 specimens are 36.84 K, 36.68 K, 37.23 K, and 36.87 K, respectively. This initial reduction in transition temperature is primarily assigned to the precipitation of non-superconducting secondary phases including MgTe and $MgCu_2$ at the grain boundaries, which enhances

impurity scattering and slightly reduces the active superconducting matrix volume fraction. However, distinct from conventional substitutional doping regimes, the critical transition temperature does not exhibit a continuous degradation trend with further increasing dopant concentration, remaining well stabilized within a narrow window between 36.6 K and 37.2 K. This stable evolution behavior convincingly demonstrates that Te and Cu atoms do not extensively substitute into the host lattice of MgB_2, thereby preserving the crystalline pristine nature inside the matrix grains.

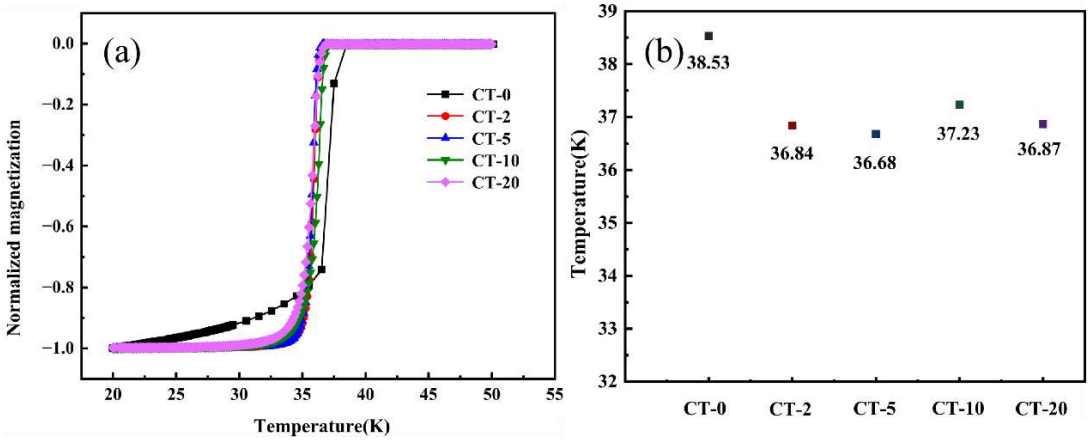


Fig. 9. (a) Reduced M-T curves and (b) comparison of T_c for the composite samples with varying Cu_2Te doping levels

Fig. 10 illustrates the J_c-H curves at 20 K for MgB_2 samples with varying Cu_2Te concentrations, derived using the Bean critical state model. Overall, J_c demonstrates a profound sensitivity to the dopant contents, exhibiting a systematic evolutionary trend characterized by low-doping enhancement and high-doping suppression.

In the low-field regime (H<2 T), superconducting current transport is fundamentally governed by intergranular connectivity and the effective superconducting cross-sectional area. As depicted in Fig. 10, the J_c curves for the CT-2 and CT-5 samples in this low-field region are markedly superior to that of the pristine MgB_2 baseline. Specifically, the self-field J_c of CT-2 reaches 2.3×10^5 A·cm^{-2}, representing a 15% enhancement over the pure sample (approximately 2.0×10^5 A·cm^{-2}). This substantial elevation firmly corroborates the preceding microstructural mechanistic analyses. Despite the presence of micro-voids in lightly doped samples observed by SEM, an appropriate amount of Mg-Cu liquid-phase reaction effectively scavenges the grain boundaries and mitigates the insulating oxide barriers. Concurrently, grain refinement escalates the grain boundary density. Synergistically, these factors ameliorate the percolation efficiency of superconducting currents across grains, thereby dramatically boosting the low-field J_c.

As the magnetic field intensifies (H>2 T), the flux pinning mechanism emerges as the paramount factor sustaining J_c. Fig. 10 unambiguously identifies 2 wt% as the optimal dopant concentration. The J_c curve of the CT-2 specimen eclipses that of the pristine sample across the entire measured field range, preserving the highest J_c even under a robust field of H=4 T. This compellingly signifies that CT-2 successfully incorporates nanoscale MgTe and $MgCu_2$ precipitates whose dimensions match the coherence length of MgB_2. These potent point-defect pinning centers act in synergy

with the refined grain boundary pinning landscape, drastically reinforcing the flux pinning force under intense magnetic fields.

Notably, while CT-5 exhibits exemplary low-field performance, its J_c curve rapidly degrades and intersects the pristine baseline once the field exceeds 2.5 T. This implies that the volumetric reduction of the superconducting MgB_2 matrix-precipitated by the proliferation of secondary phases in the CT-5 sample-begins to outweigh the beneficial effects of enhanced pinning. Hence, carefully tailoring the dopant amount is pivotal for optimizing superconducting performance. Upon escalating the doping levels to 10 wt% and 20 wt%, J_c suffers a catastrophic degradation across all field ranges. Correlated with the EDS and SEM characterizations (see Fig. 5), this severe deterioration stems from the extensive agglomeration of non-superconducting secondary phases at the grain boundaries. These segregations form continuous insulating barriers that sever the effective superconducting percolation pathways, culminating in a complete collapse of the current-carrying capacity.

Ultimately, the optimally doped CT-2 sample achieves a masterful dual optimization of intergranular connectivity and flux pinning capacity, yielding unparalleled comprehensive superconducting properties. Exceeding this critical threshold inevitably compromises intergranular connectivity due to excessive impurity incorporation, triggering a rapid deterioration in superconducting performance.

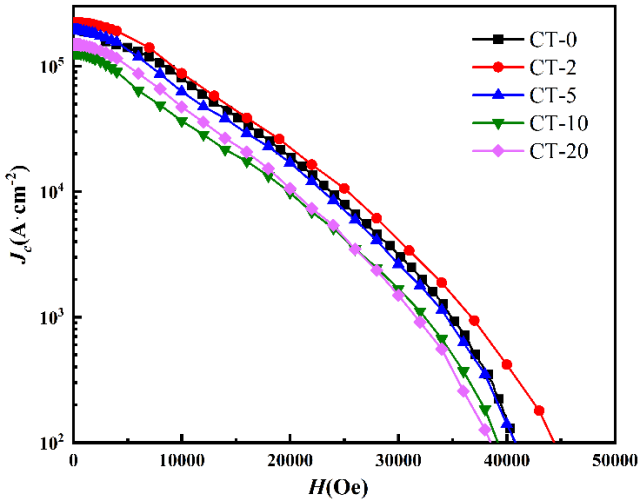


Fig. 10. Critical current density (J_c) as a function of magnetic field for the composite samples with varying Cu_2Te doping levels

To unravel the intrinsic influence of Cu_2Te doping on the flux pinning mechanisms and to pinpoint the microphysical origins driving the J_c enhancement, the magnetic field dependence data were normalized using the Dew-Hughes scaling law. Fig. 11 presents the profiles of the normalized pinning force density ($f=F_p/F_{p,max}$) against the reduced magnetic field ($h=H/H_{irr}$) at 20 K, with H_{irr} defined as the irreversibility field at a J_c criterion of 100A·cm^{-2}. Dictated by the Dew-Hughes framework, distinct topologies of pinning centers manifest as specific peak positions (h_{peak}) in the $f(h)$ curves. Specifically, point pinning (e.g., localized lattice defects or intragranular nanoprecipitates) theoretically yields an h_{peak} at approximately 0.33, while surface pinning (e.g., grain boundaries or planar faults) is characterized by an h_{peak} at approximately 0.2.

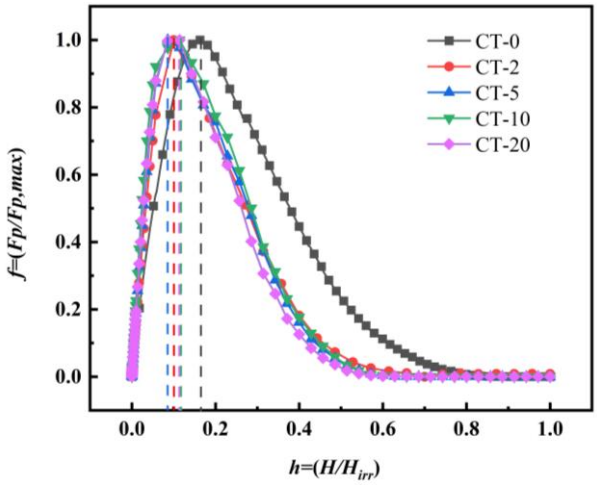


Fig. 11. Variation of reduced pinning force density with magnetic field for Cu_2Te doped MgB_2 samples at 20 K

As unequivocally depicted in Fig. 11, the peak positions (h_{peak}) for the pristine MgB_2 and all Cu_2Te-doped variants persistently fall within the 0.1 - 0.15 regime, falling significantly below the 0.2 threshold. This signature compellingly dictates that grain boundary pinning-synonymous with surface pinning-remains the ubiquitous, dominating mechanism governing the flux pinning behavior across this system. This conclusion perfectly corroborates the pronounced grain refinement detected via XRD and the dense intergranular networks visualized in SEM. Essentially, the dopant-induced grain refinement drastically amplifies the specific grain boundary area, furnishing the predominant flux pinning sources. A meticulous comparative analysis unveils a subtle but systematic correlation between microstructural evolution and the macroscopic peak shift. With increasing dopant concentration, h_{peak} progressively migrates toward lower reduced fields: shifting from $h\approx0.15$ for pure MgB_2 to $h\approx0.12$ for CT-5, and further descending below $h<0.1$ for the heavily doped CT-20. Such a "leftward shift" paradigm typically signifies an overwhelmingly high density of grain boundaries or 2D defects that exert exceptionally robust pinning at low fields but are highly susceptible to thermally activated flux creep at elevated fields. Notably, the extreme descent of h_{peak} below 0.1 serves as a quantitative signature for this drastically exacerbated creep sensitivity. According to flux pinning theory, while an overabundance of pinning centers-particularly the massive proliferation of non-superconducting secondary grain boundaries-furnishes ample pinning sites at low fields, these interfaces simultaneously act as preferential channels for the thermally activated hopping of flux lines. Consequently, as the applied magnetic field intensifies, these dense intergranular networks readily morph into active flux creep pathways. This effectively suppresses the pinning potential barrier, thereby exacerbating the J_c attenuation in the high-field regime.

The J_c-H profiles (Fig. 10) of the variedly doped specimens compellingly corroborate this mechanism. Exclusively, the CT-2 sample exhibits a superior J_c across the entire field range relative to the pristine baseline, successfully striking an optimal balance between pinning enhancement and creep suppression. Conversely, the high-field attenuation behaviors among the more heavily doped variants diverge significantly.

Although CT-5 maintains an appreciable current-carrying capacity at low fields, its J_c decay rate accelerates markedly as the field escalates (H>2.5 T). The CT-10 and CT-20 specimens display progressively steeper decay trajectories, culminating in severe global performance degradation. This macroscopic trend aligns well with the observation in Fig. 11 that the h_{peak} values of all doped samples exhibit a leftward shift. The microstructural underpinning for these discrepancies lies in the fact that, once the Cu_2Te doping exceeds the optimal threshold (2 wt%), excessive non-superconducting $MgCu_2$ and MgTe phases aggressively agglomerate at the grain boundaries, forming continuous insulating barrier layers. This detrimental microstructural architecture not only severs the percolation pathways for superconducting currents but also introduces a massive volume of interfacial regions with suppressed pinning potentials. Consequently, magnetic flux lines become highly susceptible to thermally activated creep, directly precipitating the rapid degradation of high-field J_c. For the CT-10 and CT-20 samples, this severe agglomeration effect is further exacerbated, dictating their exceptionally steep high-field decay slopes. This fundamental trade-off elucidates that an optimal dopant concentration (2 wt% Cu_2Te) precisely strikes the ultimate balance between multiplying pinning center density and mitigating flux creep; beyond this critical threshold, exacerbated flux creep overwhelmingly dominates the performance deterioration. Integrating these macroscopic findings with the TEM characterizations provides profound mechanistic insight: although the precipitation of MgTe and $MgCu_2$ nanoparticles should theoretically introduce point pinning (thereby shifting the peak rightward), EDS mapping (Fig. 5) confirms their exclusive segregation at the grain boundaries. Consequently, a unique synergistic pinning architecture is established. The dopant-induced nanoprecipitates do not act as isolated intragranular “point pinning centers”; rather, they intimately decorate and fortify the existing grain boundaries. This interfacial modification exponentially amplifies the low-field pinning force, elegantly elucidating the explosive surge in low-field J_c (CT-5 and CT-10 in Fig. 10). Conversely, this architecture also precipitates a more rapid attenuation of the pinning force at high fields, explaining the steeper high-h descent of the doped samples relative to the pristine baseline.

Ultimately, Cu_2Te doping fundamentally preserves the grain boundary-dominated pinning nature of MgB_2. However, it masterfully engineers the microstructural landscape through a dual synergistic mechanism: multiplying the quantity of pinning sites via grain refinement and amplifying the pinning quality via intergranular nanoprecipitation. This synergistic orchestration substantially elevates the maximum pinning force density ($F_{p,max}$), thereby unlocking superior comprehensive superconducting performance.

4. Conclusion

This study comprehensively reveals the microstructural, kinetic, and electromagnetic regulatory mechanisms governing Cu_2Te-doped MgB_2 superconductors fabricated via an in-situ solid-state sintering. The DSC thermodynamic analysis demonstrates that the incorporation of Cu_2Te significantly alters the reaction pathway of MgB_2. It shows that the Mg-Cu eutectic liquid phase acts as a high-speed

diffusion conduit, accelerating the transport of Mg atoms and thereby depressing the primary phase formation temperature of MgB_2 by approximately 50 ℃. Crucially, this low-temperature liquid-assisted reaction mechanism not only facilitates robust sintering densification but also effectively suppresses excessive grain overgrowth, laying a solid foundation for the formation of a high-performance microstructural architecture.

Multi-scale microstructural characterizations unambiguously confirm that the enhanced superconducting performance is underpinned by the synergistic operation of a dual microstructural mechanism. First, the transient liquid phase refines the intergranular boundaries, streamlining the percolation pathways for superconducting currents. Second, the in-situ precipitation of MgTe and $MgCu_2$ nanoparticles (10-50 nm) yields a dense dispersion of point defects perfectly matching the MgB_2 coherence length, which act as potent pinning centers to drastically elevate high-field current-carrying capabilities. Conversely, the doping level over 10 wt% induces detrimental step-like grain coarsening and severe intergranular agglomeration of non-superconducting secondary phases, which brutally sever the conductive percolation networks. Ultimately, delicately balancing the competition between liquid-phase activated densification and impurity-induced barrier formation is imperative for synthesizing advanced Cu_2Te-doped MgB_2 superconductors.

Funding

This work was supported by the National Natural Science Foundation of China (52374397).

Acknowledgments

This work was supported by the National Natural Science Foundation of China (52374397). The authors thank Qian Zhao, Hang Shen, Yan Xue, Guoqing Xia, Jiabo Zhang, Shilong Ma, Hao Liang, Yaran Zhang for their support.

References

[1] J. Nagamatsu, N. Nakagawa, T. Muranaka, Y. Zenitani, J. Akimitsu, Super conductivity at 39 K in magnesium diboride, Nature. 410 (2001) 63-64, htt ps://doi.org/10.1038/35065039.

[2] C. Buzea, T. Yamashita, Review of superconducting properties of MgB_2, S upercond. Sci. Technol. 14 (2001) R115-R146, https://doi.org/10.1088/0953-2 048/14/11/201.

[3] Q. Wang, L. Li, Y. Zhao, H. Zhang, Y. Zhang, The effects of sintering te mperature on superconductivity of MgB_2 prepared by hot pressing, Int. J. Mod. Phys. B. 34 (2020) 2050012, https://doi.org/10.1142/S0217979220500 125.

[4] Y Takahashi, T Naito, H Fujishiro, Critical current properties of an ex-situ MgB_2/TiB_2 sample fabricated by spark plasma sintering using MgB_2 powder containing TiB_2, Physica C 604 (2023), 0921-4534,

https://doi.org/10.1016/j.physc.2022.1354143.

[5] Y. Shimada, Y. Kubota, S. Hata, K. Ikeda, H. Nakashima, A. Matsumoto, K. Togano, J. Hur, H. Kumakura, Microstructure in high-density MgB_2 wires prepared by an internal Mg diffusion method, IEEE Trans. Appl. Supercond. 21 (3) (2011) 2668-2671, https://doi.org/10.1109/TASC.2010.2091097.

[6] W.K. Yeoh, S.X. Dou, Enhancement of H_{c2} and J_c by carbon-based chemical doping, Physica C 456 (1-2) (2007) 170-179, https://doi.org/10.1016/j.physc.2007.01.024.

[7] Z.L Gao, S. Santra, S. Amirkhanlou, E. Eardley, C. Wort, C.R.M. Grovenor, S. C. Speller, Microstructures and superconducting properties of MgB_2 bulk samples processed by ultra-high pressure-assisted sintering, J. Eur. Ceram. Soc. 42 (2022) 7481-7490, https://doi.org/10.1016/J.JEURCERAMSOC.2022.09.008.

[8] D. Gajda, A. Morawski, A. J. Zaleski, W. Häßler, K. Nenkov, M. A. Rind fleisch, E. Żuchowska, G. Gajda, T. Czujko, T Cetner, M. S. A. Hossain, The critical parameters in in-situ MgB_2 wires and tapes with ex-situ MgB_2 barrier after hot isostatic pressure, cold drawing, cold rolling and doping, J. Appl. Phys. 117 (2015) 173908, http://dx.doi.org/10.1063/1.4919364.

[9] T. Cetner, A. Morawski, K. Adamczyk, M. Rindfleisch, M. Tomsic, A. Zal eski, D. Gajda, A. Presz, Improvement of critical properties of undoped, multifilamentary MgB_2 wires in Nb/Cu after annealing under high gas pres sure, High Press. Res. 32 (2012) 419-424, https://doi.org/10.1080/08957959. 2012.722211.

[10] D. Gajda, Analysis Method of High-Field Pinning Centers in NbTi Wires and MgB_2 Wires, J. Low Temp. Phys. 194 (2019) 166-182, https://doi.org/ 10.1007/s10909-018-2076-z.

[11] F.A. Salem, Grain boundary effects and AC-susceptibility measurements in aluminum-doped MgB_2 superconductor, J. Supercond. Nov. Magn. 27 (2014) 2707-2711,https://doi.org/10.1007/s10948-014-2816-5.

[12] R.J. Cava, H.W. Zandbergen, K. Inumaru, The substitutional chemistry of MgB_2, Physica C 385 (2003) 8-15, https://doi.org/10.1016/S0921-4534(02)02 327-4.

[13] G. Sharma, S. Sharma, Theoretical study of superconducting parameters of Al and Li Co-doping substitution on MgB_2, Mater. Today Proc. 66 (2022) 3340-3343, https://doi.org/10.1016/j.matpr.2022.06.541.

[14] T. Masui, Transport properties and Raman spectra of impurity substituted MgB_2, Physica C 456 (2007) 102-107, https://doi.org/10.1016/j.physc.2007.0 1.022.

[15] W.X. Li, J.X. Kang, S.W. Fu, Y.M. Hu, P.F. Hu, M.Y. Zhu, Y. Li, Rare e arth doping effects on superconducting properties of MgB_2: a review, J. R are Earths 37 (2019) 124-133, https://doi.org/10.1016/j.jre.2018.05.010.

[16] A. Agostino, M. Panetta, P. Volpe, M. Truccato, S. Cagliero, L. Gozzelino , R. Gerbaldo, G. Ghigo, F. Laviano, G. Lopardo, B. Minetti, Na substitut ion effects on MgB_2 synthesized with a microwave-assisted technique, IEE E Trans. Appl. Supercond. 17 (2007) 2774-2777, https://doi.org/10.1109/TA SC.2007.900046.

[17] H. Fujii, A. Ishitoya, S. Itoh, K. Ozawa, H. Kitaguchi, Effect of additions of Ca compounds to the filling powder on the reduction of MgO and the critical current density properties of ex situ processed MgB_2 tapes, J. Allo ys Compd. 664 (2016) 650-656. https://doi.org/10.1016/j.jallcom.2016.01.027 .

[18] T. Naito, T. Yoshida, H. Fujishiro, Ti-doping effects on magnetic propertie s of dense MgB_2 bulk superconductors, Supercond. Sci. Technol. 28 (2015) 9, https://doi.org/10.1088/0953-2048/28/9/095009.

[19] M. Shahabuddin, N.S. Alzayed, N.A. Madhar, S.A. Qaid, S.M. Ramay, Im pact of carbon-based doping on the structural and superconducting properti es of MgB_2: a comparative study, J. Supercond. Novel Magn. 38 (2025) 1 02. https://doi.org/10.1007/s10948-025-06942-7.

[20] S.X. Dou, A.V. Pan, S. Zhou, M. Ionescu, H.K. Liu, Substitution induced pinning in MgB_2 superconductor doped with SiC nano-particles, Supercond. Sci. Technol. 15 (2002) 1587–1591, https://doi.org/10.1088/0953-2048/15/1 1/317.

[21] S.X. Dou, O. Shcherbakova, W.K. Yeoh, J.H. Kim, S. Soltanian, X.L. Wa ng, C. Senatore, R. Flukiger, M. Dhalle, O. Husnjak, E. Babic, Mechanis m of enhancement in electromagnetic properties of MgB_2 by nano SiC do ping, Phys. Rev. Lett. 98 (2007) 097002, https://doi.org/10.1103/PhysRevLet t.98.097002.

[22] S.F. Wang, S.Y. Dai, Y.L. Zhou, Z.H. Chen, Effect of Cd doping on struc ture and superconductivity in $Mg_{0.5}Cd_{0.5}B_2$, J. Supercond. 17 (2004) 397-40 0, https://doi.org/10.1023/B:JOSC.0000034265.53975.d4.

[23] M. Muralidhar, K. Inoue, M.R. Koblischka, M. Murakami, Critical current densities in Ag-added bulk MgB_2, Physica C 518 (2015) 36-39, https://doi. org/10.1016/j.physc.2015.02.042.

[24] S.K. Chen, Z. Lockman, M. Wei, B.A. Glowacki, J.L. MacManus-Driscoll, Improved current densities in MgB_2 by liquid-assisted sintering, Appl. Phys . Lett. 86 (2005) 242501. https://doi.org/10.1063/1.1947374.

[25] Z.Q. Ma, Y.C. Liu, Q.Z. Shi, Q. Zhao, Z.M. Gao, The mechanism of acc elerated phase formation of MgB_2 by Cu-doping during low-temperature si ntering, Mater. Res. Bull. 44 (2009)531-537. https://doi.org/10.1016/j.materr esbull.2008.07.011.

[26] Y. Zhao, D.X. Huang, Y. Feng, C.H. Cheng, T. Machi, N. Koshizuka, M.

Murakami, Nanoparticle structure of MgB_2 with ultrathin TiB_2 grain boundaries, Appl. Phys. Lett. 80 (2002) 1640-1642, https://doi.org/10.1063/1.1456969.

[27] Q. Zhao, Y.C. Liu, Q. Cai, Analysis of the precipitation process of secondary phase $MgNi_{2.5}B_2$ and superconducting properties in Ni-doped MgB_2 bulk, Mater. Chem. Phys. 138 (2013) 192-198, https://doi.org/10.1016/j.matchemphys.2012.11.043.

[28] Q. Zhao, S.L. Ma, G.Q. Xia, J.B. Zhang, Y.R. Zhang, The fabrication of graphene supported Ni nanoparticles and its doping influence on the microstructure and superconductivity of MgB_2, Physica C 627 (2024) 1354615, https://doi.org/10.1016/j.physc.2024.1354615.

[29] Q. Zhao, J.B. Zhang, G.Q. Xia, S.L. Ma, S.F. Fan, X.C. Ping, L. Hao, Y. R. Zhang, Influence of Cu_2Se doping on the morphology, structure and synthesis reactions in MgB_2 material, J. Alloys Compd. 1010 (2025) 178224, https://doi.org/10.1016/j.jallcom.2024.178224.

[30] C.P. Bean, Magnetization of hard superconductors, Phys. Rev. Lett. 8 (1962) 250-253, https://doi.org/10.1103/PhysRevLett.8.250.

[31] N. Varghese, K. Vinod, S. Rahul, K.M. Devadas, S. Thomas, S. Pradhan, U. Syamaprasad, Influence of nano-Cu additive on MgB_2 phase formation, processing temperature, and transport properties, J. Appl. Phys. 109 (2011) 033902, https://doi.org/10.1063/1.3544067.

[32] H.Y. Zhai, H.M. Christen, L. Zhang, M. Paranthaman, C. Cantoni, B.C. Sales, P.H. Fleming, D.K. Christen, D.H. Lowndes, Growth mechanism of superconducting MgB_2 films prepared by various methods, J. Mater. Res. 16 (2001) 2759-2762. https://doi.org/10.1557/JMR.2001.0375.

Statements & Declarations

☒ The authors declare that they have no known competing financial interests or personal relationships that could have appeared to influence the work reported in this paper.

☐ The authors declare the following financial interests/personal relationships which may be considered as potential competing interests:

Supplementary Files

This is a list of supplementary files associated with this preprint. Click to download.

- PrimeNoveltyStatement.docx
- Highlights.docx
- GraphicalAbstract.docx